K-Nearest Neighbor Based Locally Connected Network for Fast Morphological Reconstruction in Fluorescence Molecular Tomography

Hui Meng, Yuan Gao, Xin Yang, Kun Wang, and Jie Tian, *Fellow, IEEE*

***Abstract*— Fluorescence molecular tomography (FMT) is a highly sensitive and noninvasive imaging modality for three-dimensional visualization of fluorescence probe distribution in small animals. However, the simplified photon propagation model and ill-posed inverse problem limit the improvement of FMT reconstruction. In this work, we proposed a novel K-nearest neighbor based locally connected (KNN-LC) network to improve the performance of morphological reconstruction in FMT. It directly builds the inverse process of photon transmission by learning the mapping relation between the surface photon intensity and the distribution of fluorescent source. KNN-LC network cascades a fully connected (FC) sub-network with a locally connected (LC) sub-network, where the FC part provides a coarse reconstruction result and LC part fine-tunes the morphological quality of reconstructed result. To assess the performance of our proposed network, we implemented both numerical simulation and *in vivo* studies. Furthermore, split Bregman-resolved total variation (SBRTV) regularization method and inverse problem simulation (IPS) method were utilized as baselines in all comparisons. The results demonstrated that KNN-LC network achieved accurate reconstruction in both source localization and morphology recovery in a short time. This promoted the *in vivo* application of FMT for visualizing the distribution of biomarkers inside biological tissue.**

***Index Terms*— Fluorescence tomography, machine learning, brain.**

Manuscript received January 15, 2020; accepted March 26, 2020. Date of publication April 3, 2020; date of current version September 30, 2020. This work was supported in part by the Science and Technology of China under Grant 2017YFA0205200, Grant 2015CB755500, and Grant 2016YFA0100902, in part by the National Natural Science Foundation of China under Grant 61671449, Grant 81930053, Grant 81227901, Grant 81871442, and Grant 81527805, in part by the Chinese Academy of Sciences under Grant KFJ-STS-ZDTP-059, Grant YJKYYQ20180048, Grant XDB32030200, and Grant QYZDJ-SSW-JSC005. *(Hui Meng and Yuan Gao contributed equally to this work.) (Corresponding authors: Kun Wang; Jie Tian.)*

Hui Meng, Yuan Gao, Xin Yang, and Kun Wang are with the CAS Key Laboratory of Molecular Imaging, Institute of Automation, Beijing 100190, China, also with the School of Artificial Intelligence, University of Chinese Academy of Sciences, Beijing 100049, China, and also with the Beijing Key Laboratory of Molecular Imaging, Beijing 100190, China (e-mail: menghui2015@ia.ac.cn; gaoyuan2014@ia.ac.cn; xin.yang@ia.ac.cn; kun.wang@ia.ac.cn).

Jie Tian is with the CAS Key Laboratory of Molecular Imaging, Institute of Automation, Beijing 100190, China, also with the Beijing Key Laboratory of Molecular Imaging, Beijing 100190, China, also with the Beijing Advanced Innovation Center for Big Data-Based Precision Medicine, Beihang University, Beijing 100191, China, also with the Engineering Research Center of Molecular and Neuro Imaging of Ministry of Education, School of Life Science and Technology, Xidian University, Xi'an 710126, China, and also with the Key Laboratory of Big Data-Based Precision Medicine, Ministry of Industry and Information Technology, Beihang University, Beijing 100191, China (e-mail: tian@ieee.org).

This article has supplementary downloadable material available at http://ieeexplore.ieee.org, provided by the authors.

Color versions of one or more of the figures in this article are available online at http://ieeexplore.ieee.org.

Digital Object Identifier 10.1109/TMI.2020.2984557

I. Introduction

FLUORESCENCE molecular imaging (FMI) is a widely applied optical imaging modality for numerous preclinical applications [1]–[3]. FMI can provide highly sensitive, highly specific and non-invasive measurements of fluorescent source in biological tissue. However, due to the absorption and scattering of light transmission [4]–[6], FMI can only obtain the photon intensity on the object surface, which does not report the three-dimensional (3D) distribution of fluorescent source inside the object. Therefore, fluorescence molecular tomography (FMT) has been developed to trace the fluorescent source location and recover the distribution of fluorescence probes [7]. However, the complexity of photon propagation model and the ill-posedness of inverse problem still limit the development of FMT reconstruction.

To alleviate the modeling error and solve the ill-posed inverse problem in FMT reconstruction, many researchers have developed different model-based methods. High-order approximation models [8], [9] were proposed to describe the photon propagation. Moreover, the priori knowledge such as structural information (magnetic resonance imaging (MRI) or computed tomography (CT)) with corresponding optical parameters was utilized to build the photon propagation model [10], [11]. Furthermore, numerous regularization terms [12]–[14] were added to the optimization methods to alleviate the ill-posedness of inverse problem. Although these methods improved the performance of FMT reconstruction, the deviation between simplified photon propagation model and actual process of light propagation still limits the accuracy of FMT reconstruction. Moreover, the model-based method [15], [16] usually solved the inverse problem by iterative optimization, which was time consuming.

Recently, machine learning-based optical tomography reconstruction [17]–[19] was proposed to avoid modeling of photon propagation. Different from the model-based method, this strategy models the inverse photon propagation directly by learning the mapping relation between the surface photon intensity and the distribution of light source [19]. Lin *et al.*

proposed an end-to-end 3D deep encoder-decoder (3D-En-Decoder) network to reconstruct fluorescent sources, and achieved accurate locating results in regular phantom. However, because of the convolution operator, the input data of Lin's network need to be mapped to a mesh constructed of size-fixed hexahedral elements, whereas the hexahedral element cannot model the boundary of the imaging object with complex surface accurately [20]. Besides, another machine learning-based method, i.e., deep convolutional neural network, gated recurrent unit, and multiple layer perception based method (DGMM) was developed to improve the quality of FMT reconstruction [18]. DGMM obtained accurate source location, but the design of DGMM was based on strong priori knowledge of fluorescent source, which limited the application of DGMM for morphological reconstruction of FMT. Furthermore, a multilayer perceptron-based inverse problem simulation (IPS) method was developed to improve the performance of bioluminescence tomography (BLT) reconstruction [17]. This method achieved accurate *in vivo* BLT reconstruction, but its over-sparse problem limited the morphological reconstruction. Thus, the morphological reconstruction of FMT based on machine learning is still an urgent challenge to be solved.

In this study, we proposed a K-nearest neighbor based locally connected (KNN-LC) network to overcome the over-sparse problem and improve the morphological reconstruction of FMT. KNN-LC network was constructed by two parts: fully connected (FC) sub-network and locally connected (LC) sub-network. The FC sub-network was trained to reconstruct a coarse result, whereas the LC sub-network was used to fine-tune the reconstructed source with residual learning strategy. To assess the performance of KNN-LC network, numerical simulation and *in vivo* studies in orthotopic glioma mouse models were performed. Split Bregman-resolved TV (SBRTV) regularization method [21] and IPS method [17] were used as baselines for comparisons. The reconstruction results demonstrated the superiority of KNN-LC network for localization and morphology recovery of fluorescent sources.

The remainder of this paper is arranged as follows: Section II introduces model-based and machine learning-based reconstruction methods, KNN-LC network-based reconstruction method, the design of data collection and *in vivo* studies, the implementation details and the evaluation index. The results of numerical simulation and *in vivo* studies are shown in Section III. The conclusion and discussion of KNN-LC network are given in Section IV.

II. Methodology

A. Model-Based FMT Reconstruction

Model-based FMT reconstruction relies on the description of light transmission in biological tissue. It commonly uses diffusion approximation equation [22] as the photon propagation model. Based on the finite element analysis [23], [24], a linear relation between the surface photon intensity and the distribution of fluorescent source inside the object can be constructed as follows:

$$\Phi = AX \tag{1}$$

where Φ represents the photon intensity on the object surface. A is the system matrix, and X denotes the distribution of fluorescent source inside the object.

The inverse estimation of (1) is usually ill-posed because the problem is normally underdetermined. In order to solve this ill-posed inverse problem, unconstrained optimization with regularization strategies is widely used[14]. The unconstrained optimization can be defined as follows:

$$\min E(\mathrm{X}) = \frac{1}{2}\|AX - \Phi\|_2^2 + \lambda R(\mathrm{X}) \tag{2}$$

where R denotes regularization terms on X and λ is the regularization parameter.

B. Machine Learning-Based FMT Reconstruction

Machine learning-based FMT reconstruction methods [17], [25] use neural network to learn the nonlinear mapping between the surface photon intensity Φ and the distribution of fluorescent source X, which can be defined as follows:

$$\min ||f_{nn}(\Phi|\theta) - X||_2^2 \tag{3}$$

where f_{nn} is the reconstruction neural network with network weight θ. The input and output of network is surface photon intensity Φ and reconstructed fluorescent source X, respectively. Furthermore, the network weight θ is iteratively updated during the network training guided by minimizing the mean square error between the actual and reconstructed fluorescent sources.

The comparisons between model-based and machine learning-based FMT reconstruction are provided in the Supplementary Material Section S.I. Supplementary materials are available in the supplementary files / multimedia tab.

C. FMT Reconstruction Based on KNN-LC Network

KNN-LC network was inspired by IPS method [17], which is the first machine-learning method used in BLT reconstruction. IPS utilized a FC network to learn the mapping relation between Φ and X. The number of FC layers in IPS method was set to four. The adjacent two layers in FC network were fully connected, and activated by rectified linear unit (ReLU) [26] to simulate the iterative process of iterative shrinkage threshold method [27]. Although IPS method achieved accurate source localization in BLT reconstruction, the over-sparse problem heavily limited the morphological reconstruction.

To overcome the over-sparse problem, we proposed a KNN-LC network that cascaded a LC sub-network to FC sub-network, and residual learning [28] was adopted to train LC sub-network. The whole FMT reconstruction using KNN-LC network can be defined as

$$\min \|f_{FC}(\Phi|\theta_1) - X\|_2^2 + \xi\|f_{LC}(X_{FC}|\theta_2) - X_{res}\|_2^2 \tag{4}$$

where f_{FC} and f_{LC} denote the process of FC sub-network and LC sub-network, respectively. θ_1 and θ_2 are the corresponding network weights. X_{FC} is the output of FC sub-network, and X_{res} is the residual value between X_{FC} and X. $\xi \in [0, 1]$ is a hyper parameter used to balance two losses, and its value was set to 0.01 in our experiment. The task of FC sub-network was to reconstruct a coarse result, whereas the LC sub-network learned the residual mapping to improve the quality of morphological reconstruction.

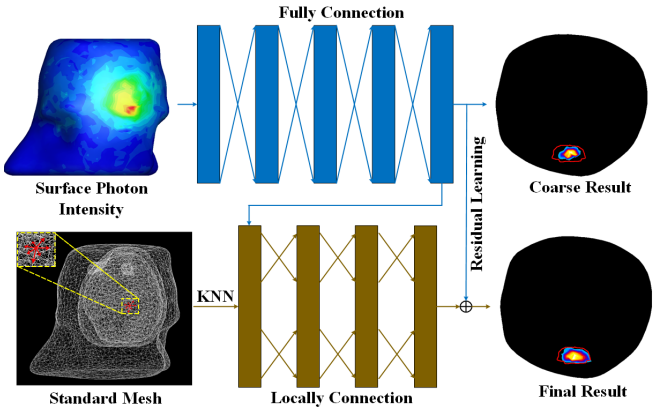

Fig. 1. Structure of KNN-LC network. FC sub-network (blue columns) performs a coarse reconstruction with the input of surface photon intensity. LC sub-network (dark yellow columns) fine-tunes the coarse result with information of KNN and residual learning. The red arrows in the standard mesh indicate the K-nearest neighbors of one vertex. Red circles in axial slices represent the ground truth of fluorescent source.

In each layer of LC sub-network, there is a one-to-one correspondence between each node in LC layers and each vertex in reconstructed results. The connection between output nodes and input nodes of LC layers was built based on an adjacency matrix, which was constructed based on Euclidean distance of vertexes and used to regularize the LC sub-network. Specifically, for each node, the K nearest neighbor nodes were considered as its adjacent nodes, whereas the others were set to be nonadjacent. LC sub-network only connected each output node with its adjacent input nodes and learned reconstructed intensity of neighbor nodes. The adjacency matrix M is defined as

$$M = (m_{i,j})_{N\times N} \tag{5}$$

$$m_{i,j} = \begin{cases} 1 & i \in S_{out} \& j \in S_{in} \& j \in S_{knn}(i) \\ 0 & i \in S_{out} \& j \in S_{in} \& j \notin S_{knn}(i) \end{cases} \tag{6}$$

where $m_{i,j}$ indicates the connection between nodes i and j. Nodes i and j are connected if $m_{i,j}$ is 1, otherwise nodes i and j are disconnected. S_{out} and S_{in} represent the node sets of the output and input layers, respectively. $S_{knn}(i)$ is the K nearest neighbor set of node i. In this study, the value of the nearest neighbor K was chosen to be 32 based on parameter test.

KNN-LC network contains four FC layers and three LC layers (Fig. 1). The network input is the photon intensity of 1609 vertexes, which are distributed on the object surface. Because we focused on the intracranial FMT reconstruction, the network output was set as the photon intensity of 1721 vertexes in permissible region (brain). The number of nodes in the hidden layers was set as 1721. Besides, a dropout function with probability 20% was applied in FC layers to reduce the over-fitting problem. The mean square error [29] and Adam algorithm (learning rate: 0.001, β_1 : 0.90, β_2 : 0.99) [30] were adopted as the loss function and the optimization function of KNN-LC network, respectively. KNN-LC network was trained with a batch size of 256 and 300 epochs.

The procedure of FMT reconstruction based on KNN-LC network is provided in the Supplementary Material Section S.II. Besides, the reconstruction results of KNN-LC networks with different FC and LC layers are presented in the Supplementary Material Section S.III.A. The performance of KNN-LC networks trained with different parameters (batch size and epoch) on validation set is presented in the Supplementary Material Section S.III.B. Furthermore, the reconstruction results of KNN-LC networks trained with different standard meshes are provided in the Supplementary Material Section S.III.C. Supplementary materials are available in the supplementary files / multimedia tab.

TABLE I
OPTICAL PARAMETERS OF MAIN ORGANS

Organ	$\mu_{ax}(mm^{-1})$	$\mu_{sx}(mm^{-1})$	$\mu_{am}(mm^{-1})$	$\mu_{sm}(mm^{-1})$
Muscle	0.0474	0.3122	0.0287	0.2427
Skull	0.0326	2.1140	0.0197	1.8541
Brain	0.0183	1.3784	0.0167	1.2156

D. Data Collection

Because KNN-LC network is a data-driven method, sufficient samples containing both surface photon intensity Φ and fluorescent source X are extremely important. However, it is unpractical to collect surface photon intensity by implementing thousands of *in vivo* experiments. Besides, the actual distribution of fluorescent sources in mice is difficult to acquire. In order to overcome these problems, we utilized the Monte Carlo (MC) method [31], [32] to collect the training data. MC has been widely used to simulate the photon transmission in biological tissue [33], [34], which can provide both surface photon intensity and gold standard of fluorescent sources. In order to simulate the *in vivo* experiments, all simulation samples were obtained using a standard mesh, which was discretized from segmented CT data of a mouse head. The standard mesh used in our experiment contained 13286 nodes and 70412 tetrahedrons. The segmented organs mainly contain muscle, skull and brain, and the corresponding optical parameters [35] are listed in Table. I.

Considering the fluorescent sources can be anywhere in mouse brain, the simulation samples should cover the brain space as much as possible. 643 single-source samples with the radius of 0.6 mm and the barycenter gap of 0.6 mm were collected using Monte Carlo simulation (MOSE v2.3) [34]. The minimum and maximum depths of single-source samples were 1.3 and 4.4 mm, respectively. For training KNN-LC network, 100 single-source samples were randomly selected as the validation set, and the remaining 543 samples were used as the training set.

Furthermore, in order to minimize the overfitting and improve the network performance, data augmentation with little calculation was adopted. Dual-source samples and big-source samples were assembled by selecting and adding the corresponding data of single-source samples. The surface photon Φ and the fluorescent source X of the assembled source samples were calculated as follows:

$$\Phi_{ass} = \sum_{i\in S_n} \Phi_i \tag{7}$$

$$X_{ass} = \sum_{i\in S_n} X_i \tag{8}$$

where Φ_{ass} and Φ_i represent the surface photon of assembled sample and the ith single-source sample, respectively. S_n is the set of selected single-source samples and n is the number of selected samples. Dual-source samples were created by randomly selecting two samples (n = 2) from the single-source samples. Big-source samples were constructed by centering on a single-source sample and assembling n nearest single-source samples (n = 10, 20, 30, 40, and 50). Besides, the nearest two assembled source samples (n = 10) were assembled to obtain more irregular shaped big-source samples.

In total, we simulated 543 single-source samples and assembled 7258 samples (4000 dual-source samples and 3258 big-source samples) to construct the training set. Similarly, another 100 simulated single-source samples, and 900 assembled samples (400 dual-source samples and 500 big-source samples) were collected to construct the validation set. Besides, three dual-source samples with different barycenter gaps, one ellipsoid shaped source sample and three big spherical source samples with different depths were produced using MOSE platform to further verify the performance of KNN-LC network.

E. In Vivo Experiment

To evaluate the utility of KNN-LC network, *in vivo* FMT reconstruction in orthotopic glioma mouse models was implemented. All animal experiments were performed under the guidelines of the Institutional Animal Care and Use Committee at Peking University. The orthotopic glioma mouse models were established following the protocols of [15], and 200 μL Tf-IRDye800 [15] were injected into each tumor-bearing mouse through the tail vein. Six hours after the injection, the surface fluorescence images and CT data were first collected using a pentamodal imaging system [36], [37] and the MRI data (M3TM, Aspect Imaging, Israel) was obtained subsequently.

In the process of optical image acquisition, the excitation light was produced by a 750 nm continuous wave semiconductor laser with 450 mW output power. The fluorescence images were captured using an electron multiplying charge coupled device (EMCCD) camera (iXonEM + 888, ANDOR, UK) with 0.5 s exposure and 4 × 4 binning. A bandpass filter with 820 ± 25 nm was utilized to collect the emission light. After the acquisition of optical images, CT data was collected to provide structural information. The fluorescence images were first mapped to the corresponding CT data, and then registered to the standard mesh [17]. Next, T2-weighted MR images were scanned with the following parameters: TE 50 ms, TR 6000 ms, slice spacing 0.1 mm, and slice thickness 0.8 mm [6].

After the *in vivo* multimodality imaging, mice were sacrificed and the frozen sections of mouse head were acquired using freezing microtome (CM1950, Leica, Germany). Then, the fluorescence images of frozen sections were captured by a live cell imaging system (AF6000 Modular System, Leica, Germany) equipped with a highly sensitive CCD camera (Princeton Instruments, ProEM 1024B). Finally, the frozen sections were stained with hematoxylin and eosin (H&E). All these *ex vivo* fluorescence images and H&E stained images were used as the gold standard of probe distribution and tumor area, respectively.

F. Implementation Details and Evaluation Index

The training and test of IPS and KNN-LC networks were implemented using Pytorch and Python 2.7. All computer operation was performed on a personal computer with a RTX 2080 Ti GPU and a 3.40 GHz Intel Core i7 CPU.

To quantitatively assess the performance of FMT reconstruction using different methods, the barycenter error (BCE) [17] and Dice index [15] were chosen as the evaluation indexes. BCE calculates the deviation between the barycenters of the reconstructed source and the actual source, which is defined as follows:

$$SC_t = \left(\sum_{i \in s_t} C_i \times x_i\right) \Big/ \sum_{i \in s_t} x_i \tag{9}$$

$$BCE = \|SC_{re} - SC_{ac}\|_2 \tag{10}$$

where SC_t is the weighted center coordinate of source s_t. C_i and x_i represent the coordinate and intensity of the ith vertex in s_t, respectively. $\|\cdot\|_2$ denotes the operator of Euclidean distance. SC_{re} and SC_{ac} are the barycenter coordinate of the reconstructed source and actual source, respectively. Furthermore, Dice index was adopted to assess the accuracy of morphology recovery in FMT reconstruction.

$$Dice = \frac{2\,|X \cap Y|}{|X| + |Y|} \tag{11}$$

where X and Y are the point sets of the reconstructed and actual fluorescent sources, respectively. The higher the Dice index, the better the morphological reconstruction.

III. Results

In this section, the performance of KNN-LC network was evaluated using numerical simulation and *in vivo* experiments. SBRTV and IPS methods were used as baselines. This section is structured as follows: The first part presents the comparisons of reconstruction results in validation set. The second and third parts present the performance of our proposed method in reconstructing MC simulated samples. The dual source samples in the second part and big-source samples in the third part were used to evaluate the locating accuracy and morphological reconstruction performance of KNN-LC network, respectively. In the fourth part, *in vivo* FMT reconstruction of probe distribution in glioma mouse models were carried out to verify the practicality of KNN-LC network. Last, the reconstruction times of three methods were collected to evaluate the reconstruction efficiency.

A. Validation Data Reconstruction

The performance of KNN-LC network was compared with SBRTV and IPS methods by reconstructing different samples in validation set. To quantitatively compare the performance of reconstruction results, the mean and standard deviation (SD) of

TABLE II
QUANTITATIVE RESULTS (MEAN ± SD) OF SMALL-SOURCE RECONSTRUCTION IN VALIDATION SET

Method	SBRTV	IPS	KNN-LC
BCE (mm)	1.12 ± 0.24	0.54 ± 0.31	0.42 ± 0.12

TABLE III
QUANTITATIVE RESULTS (MEAN ± SD) OF DUAL-SOURCE RECONSTRUCTION IN VALIDATION SET

Method	SBRTV	IPS	KNN-LC
BCE1 (mm)	2.25 ± 0.56	0.76 ± 0.45	0.55 ± 0.27
BCE2 (mm)	2.50 ± 0.54	0.77 ± 0.45	0.55 ± 0.28
Total BCE (mm)	4.75 ± 0.67	1.53 ± 0.73	1.11 ± 0.34

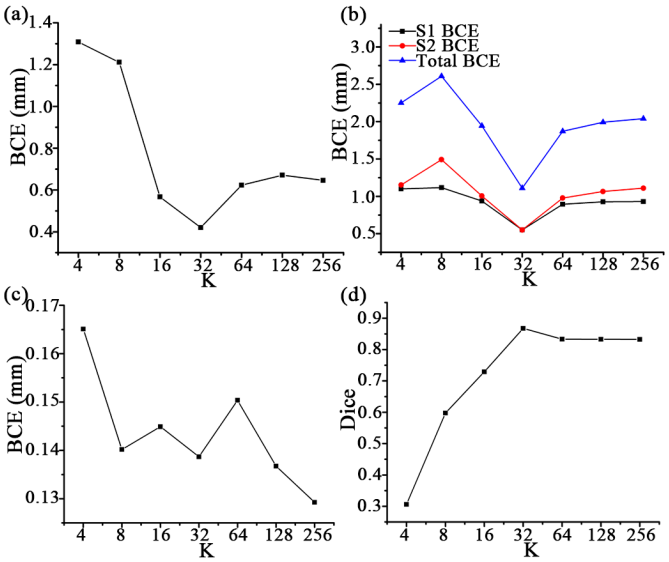

Fig. 2. Quantitative comparison of parameter K test in validation set. The average BCE of single-source reconstruction (a) and dual-source reconstruction (b). The average BCE (c) and the average Dice (d) of big-source reconstruction.

TABLE IV
QUANTITATIVE RESULTS (MEAN ± SD) OF BIG-SOURCE RECONSTRUCTION IN VALIDATION SET

Method	SBRTV	IPS	KNN-LC
BCE (mm)	1.35 ± 0.29	0.53 ± 0.06	0.14 ± 0.02
Dice	0.31 ± 0.05	0.70 ± 0.05	0.87 ± 0.02

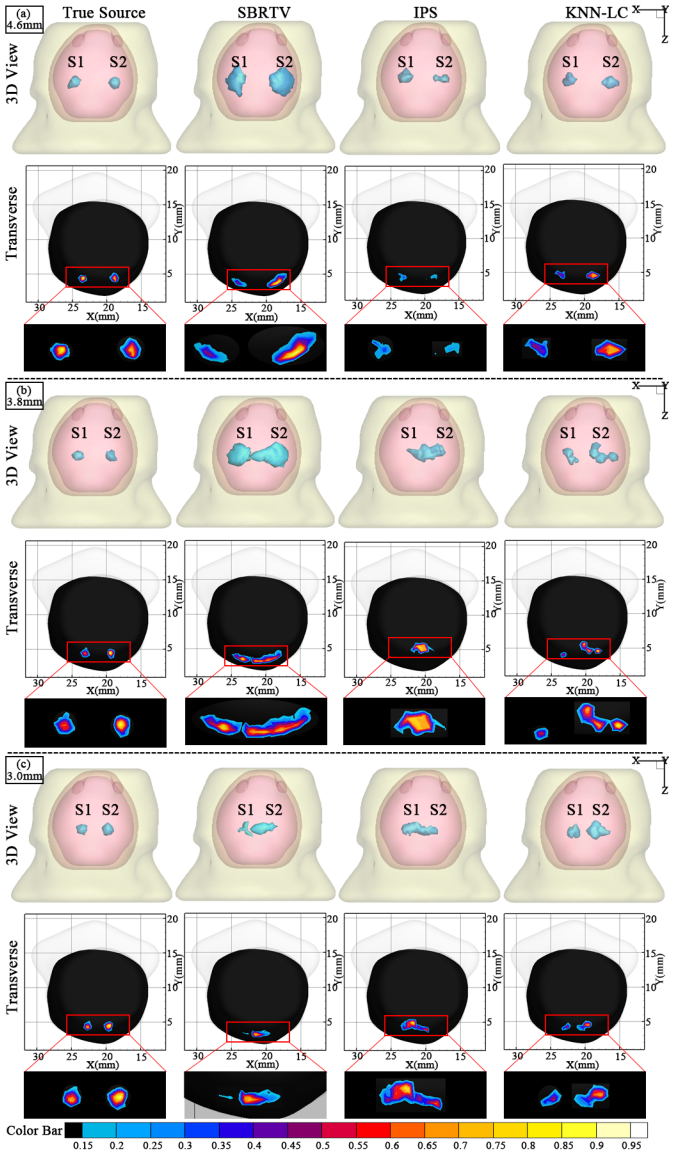

Fig. 3. FMT reconstruction results of dual sources with different barycenter gaps. (a-c) show the true and the reconstructed sources given by different methods when barycenter gap is 4.6, 3.8 and 3.0 mm, respectively. Both 3D rendering and 2D transverse sections are shown for comparisons.

BCE and Dice are presented in Table II (single-source reconstruction) and Table III (dual-source reconstruction). Both tables showed that KNN-LC network obtained the minimum BCE, which proved the capability of KNN-LC network in achieving accurate source localization. Furthermore, in big-source reconstruction (Table IV), KNN-LC network achieved the minimum BCE (0.14) and the highest Dice (0.87), which indicated the superiority of KNN-LC network for morphological reconstruction. These results demonstrated that KNN-LC network achieved more accurate source localization and morphology recovery than the other methods.

Furthermore, the value of nearest neighbor K was determined based on the results of KNN-LC network in validation samples. Fig. 2 shows quantitative reconstruction results of KNN-LC network with different K. Fig. 2(a) and Fig. 2(b) present BCE of single-source and dual-source reconstructions, respectively. Fig. 2(c) and Fig. 2(d) show average BCE and Dice of big-source reconstruction. The BCE of single-source and dual-source reconstructions first decreased and then increased with increasing K, and the minimum BCE was achieved when K = 32. In big-source reconstruction, the average BCE was 0.14 when K was 32, which was close to the minimum BCE (0.13) when K was 256. KNN-LC network obtained the maximum Dice (0.87) when K was 32 (Fig. 2(d)). All these results demonstrated that KNN-LC network with K = 32 could provide better results in both source localization and morphology recovery. Thus, we set K of KNN-LC network as 32 in all the reconstruction.

B. Dual-Source Reconstruction

The reconstruction of dual-source samples directly simulated by MC was implemented to further assess the localization

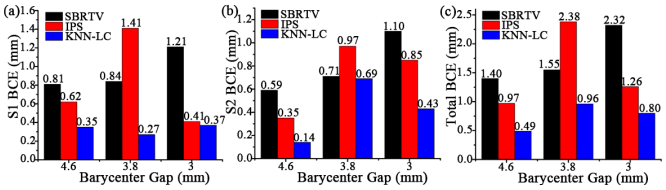

Fig. 4. Quantitative analysis of dual-source reconstruction with barycenter gap varying from 4.6 to 3 mm. (a) and (b) present the BCE of reconstructed sources S1 and S2, respectively. (c) shows the total BCE of S1 and S2.

accuracy of KNN-LC network. Three dual-source samples with different barycenter gaps were collected using MOSE platform. The radius of sources were 0.6 mm, and the barycenter gaps were set as 4.6, 3.8 and 3 mm. These dual-source samples were only used as test samples, and did not appear in the network training.

Fig. 3 shows 3D rendering and transverse section of dual-source samples with different barycenter gaps reconstructed by different methods. The transverse sections crossing both source centers (Z = 7 mm) were selected for presentation. The corresponding BCE quantification are presented in Fig. 4. All methods could distinguish two sources when the barycenter gap was 4.6 mm (Fig. 3(a)), whereas IPS and SBRTV methods failed to reconstruct two sources when the barycenter gap was 3.8 (Fig. 3(b)) or 3 mm (Fig. 3(c)). However, KNN-LC network achieved good dual-source reconstruction. Furthermore, the quantitative comparisons (Fig. 4) showed that the total BCE of KNN-LC network was 36.5%-65.5% less than that of the other two methods. These results revealed the superiority of KNN-LC network for tracing sources and distinguishing dual sources with close gaps.

To evaluate the anti-noise ability of KNN-LC network, dual-source reconstruction with 15% Gaussian noise in surface photon density was implemented. Fig. 5 presents the reconstructed results in 3D rendering and transverse section images of different methods. Consistent with no noise interfered dual-source reconstruction, IPS and SBRTV failed to reconstruct dual sources when barycenter gap was narrower than 4.6 mm, whereas KNN-LC network could distinguish dual sources when barycenter gap reached 3.0 mm. The quantitative BCE of dual-source reconstruction with noise interference is shown in Fig. 6. With the barycenter gap reduced from 4.6 to 3.0 mm, the total BCE of SBRTV method and KNN-LC network increased slightly, but that of IPS method presented unstable performance. The total BCE of KNN-LC network was 47.3%-64.9% less than that of SBRTV with barycenter gap reduced from 4.6 to 3 mm. Besides, KNN-LC network reconstructed the results with a 40.7%-72.0% lower BCE than IPS method in 4.6 and 3.8 mm dual-source reconstruction, and it achieved the similar locating performance in reconstruction with 3 mm gap. These comparisons proved that KNN-LC network achieved accurate source localization with noise interference.

C. Big-Source Reconstruction

The FMT reconstruction of MC simulated big-source samples was implemented to evaluate the performance of KNN-LC

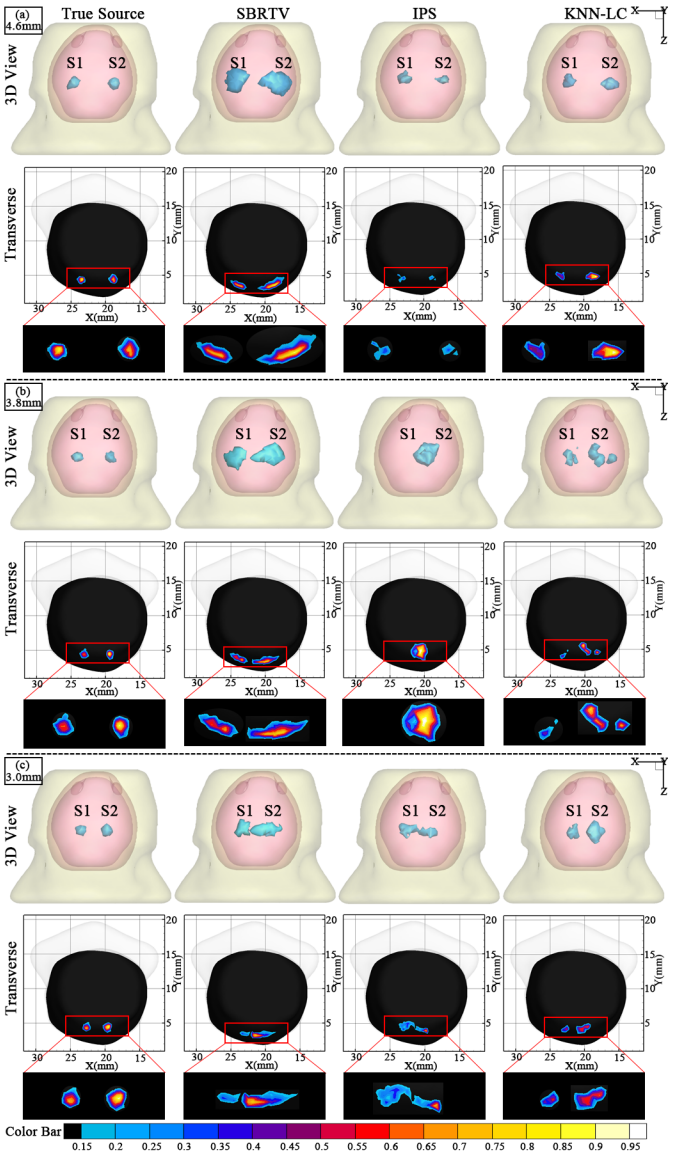

Fig. 5. FMT reconstruction results of dual sources with 15% Gaussian noise interference. (a-c) show 3D rendering and transverse sections of true and reconstructed sources given by different methods when barycenter gap varied from 4.6 to 3.0 mm.

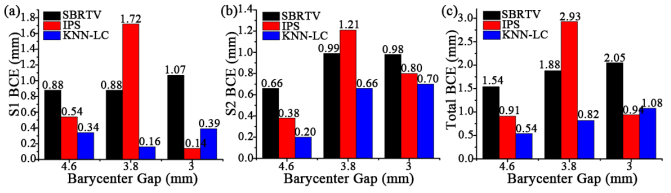

Fig. 6. Quantitative results of dual-source reconstruction with 15% Gaussian noise interference. (a-c) present S1 BCE, S2 BCE and total BCE of three methods when barycenter gap is 4.6, 3.8 and 3.0 mm, respectively.

network in morphology recovery. An ellipsoid shaped source sample was created to assess the capability of reconstructing irregular shaped source, and three big spherical source samples with different depths were collected to test the performance in deep source reconstruction. The depth of ellipsoid shaped source was 2 mm, and its axis lengths along x, y, and z axes were 1.5, 0.8 and 0.8 mm, respectively. For spherical source

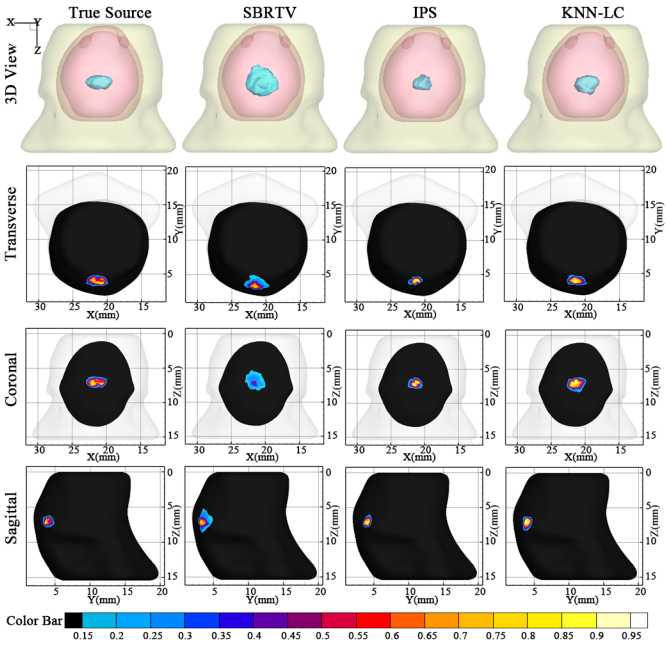

Fig. 7. FMT reconstruction results of ellipsoid shaped source using different approaches. The 3D rendering, transverse sections, coronal sections and sagittal sections of true and reconstructed sources given by SBRTV, IPS and KNN-LC, respectively.

TABLE V
QUANTITATIVE RESULTS OF THREE METHODS IN THE ELLIPSOID SHAPED SOURCE RECONSTRUCTION

Method	BCE (mm)	Dice
SBRTV	0.39	0.54
IPS	0.17	0.68
KNN-LC	0.21	0.81

(1 mm radius) samples, the depths between source barycenter and object surface were 2.2, 3.2 and 4.2 mm. All these samples were directly produced by MOSE platform, and only used as test samples.

Fig. 7 shows the 3D rendering and two-dimensional (2D) section images of ellipsoid shaped source reconstructed by three methods. The result of SBRTV was over-smooth, whereas that of IPS was over-sparse. By contrast, the reconstructed source of KNN-LC network was more like ellipsoid, which was close to the true source. Besides, the BCE and Dice of reconstruction results given by three methods are listed in Table V. SBRTV provided the largest BCE (0.39 mm), which was 1.86-2.29 times that of KNN-LC network (0.21 mm) and IPS method (0.17 mm). Besides, KNN-LC network obtained the highest Dice (0.81), which was 1.50 times that of SBRTV (0.54), as well as 1.19 times that of IPS (0.68). These results demonstrated that KNN-LC network achieved accurate morphology recovery of irregular shaped source.

The 3D rendering and transverse section images of reconstructed spherical sources are presented in Fig. 8. The reconstructed sources of SBRTV were attached to the object surface, which indicated that SBRTV failed to reconstruct the depth of fluorescent sources in these cases. Although IPS achieved deep source reconstruction, the location deviations between reconstructed and true sources were larger than those of KNN-LC

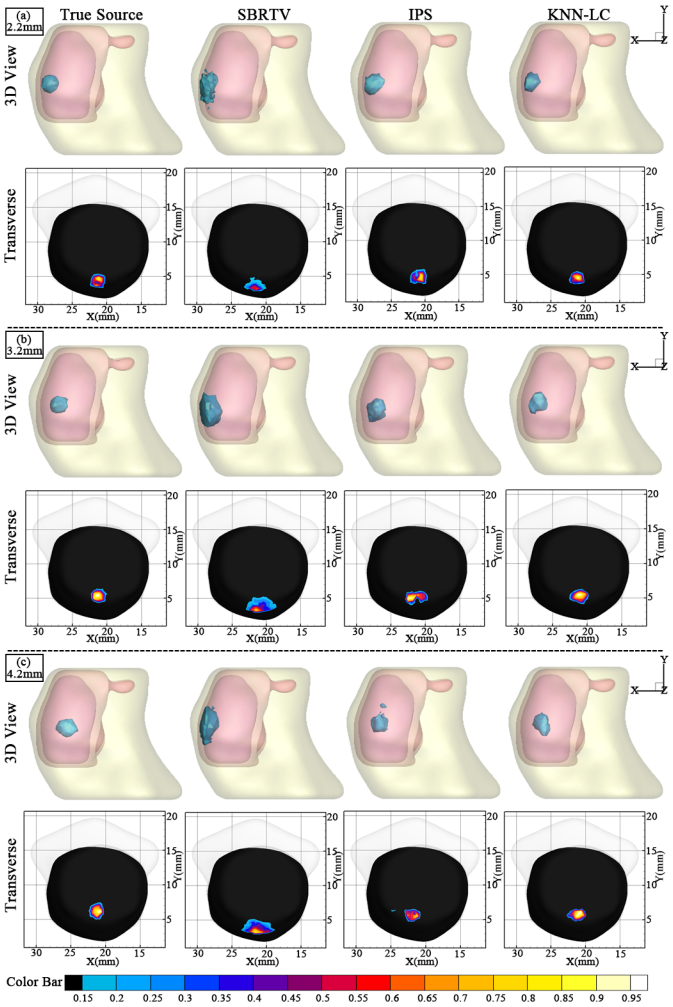

Fig. 8. FMT reconstruction results of big spherical fluorescent sources at different depths. The 3D rendering and transverse sections of true and reconstructed sources at the depths of 2.2 mm (a), 3.2 mm (b) and 4.2 mm (c).

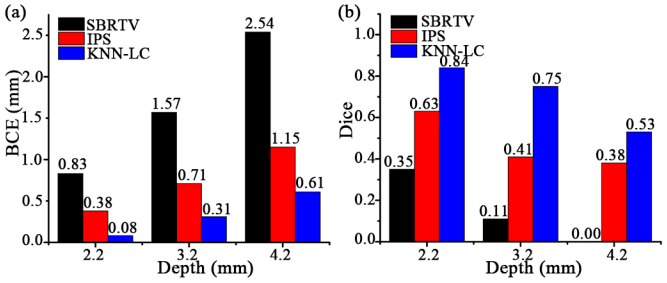

Fig. 9. Quantitative results of big spherical source reconstruction using three methods. (a) and (b) present BCE and Dice of reconstructed sources at depths of 2.2, 3.2 and 4.2 mm.

network. As shown in Fig. 9(a), KNN-LC network achieved the minimum BCE in each fluorescent source reconstruction. Besides, KNN-LC network obtained the highest Dice of 0.84, 0.75, and 0.53 at the depths of 2.2, 3.2, and 4.2 mm, respectively (Fig. 9(b)). These results revealed the superiority of KNN-LC network for morphological reconstruction of deep fluorescent sources.

In addition to these results, the performance of KNN-LC network was verified using another three ellipsoid shaped

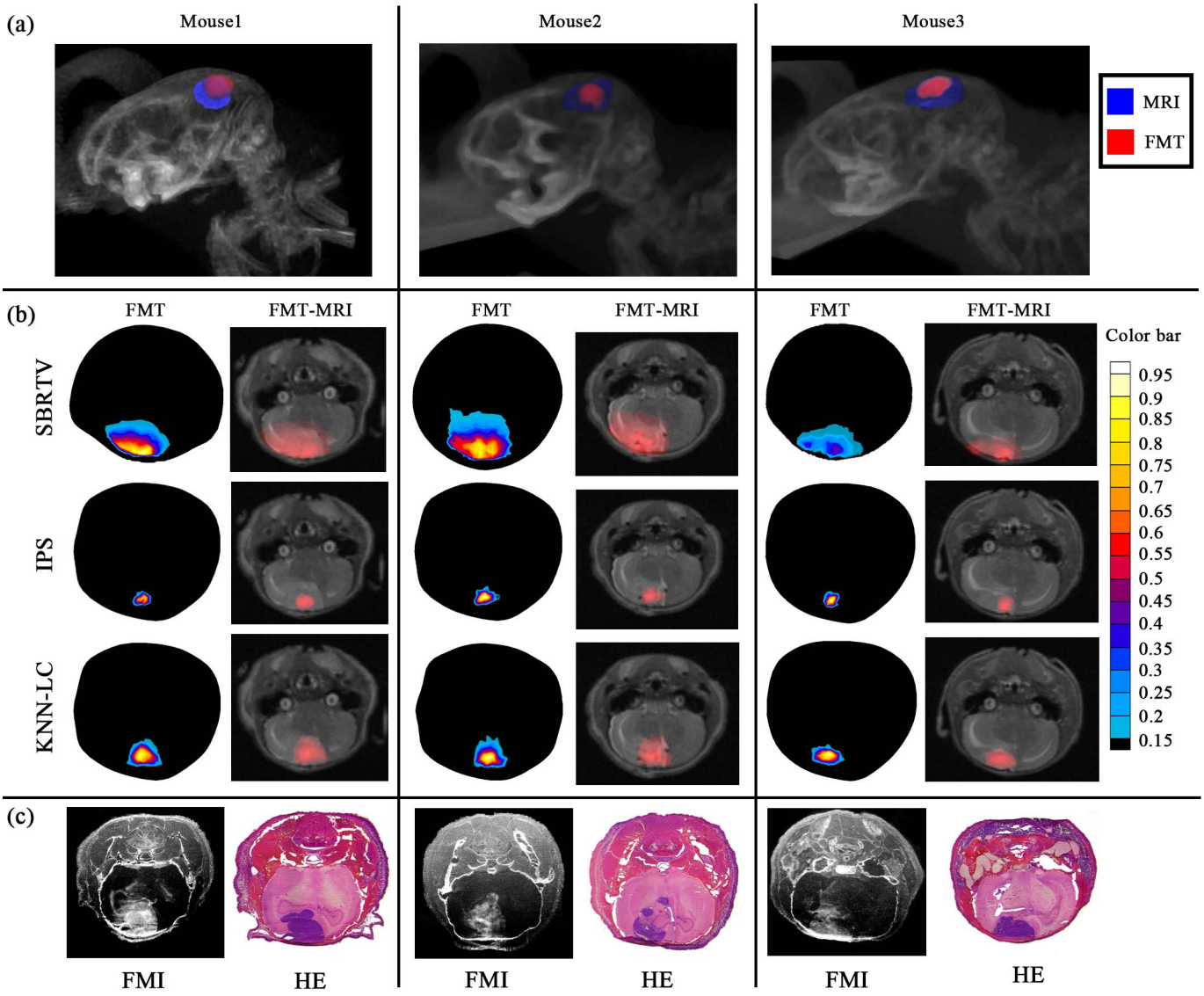

Fig. 10. *In vivo* FMT reconstruction in three orthotopic glioma bearing mice. (a) 3D rendering of KNN-LC network reconstruction results (red region) fused with segmented tumor from MRI (blue region) and CT. (b) 2D transverse sections of FMT and FMT-MRI fused images obtained using three methods. (c) Near infrared fluorescence images and the corresponding H&E stained images of frozen sections.

source samples of different source sizes, as detailed in the Supplementary Material Section S.IV. Supplementary materials are available in the supplementary files / multimedia tab.

D. In Vivo Experiment

In vivo FMT reconstruction in three glioma mouse models [15] was implemented to assess the practicability of KNN-LC network. The reconstructed results of three mice were merged with the corresponding MRI data by the maximum mutual information registration [38].

The 3D rendering of CT images with reconstructed sources of KNN-LC network (red) and segmented MRI signals (blue) are shown in Fig. 10(a). Where the reconstructed fluorescent sources and the corresponding MRI data presented the same spatial location. Besides, the transverse section images of FMT reconstruction results and merged images of FMT and MRI data are presented in Fig. 10(b). Consistent with the simulation experiments, the reconstruction results of SBRTV were over-smooth and attached to the object surface. Compared with *ex vivo* fluorescence images (Fig. 10(c)), the fluorescent sources reconstructed by IPS were over-sparse, whereas KNN-LC network overcame the over-sparse problem and obtained more accurate morphological information.

For quantitative analysis, Dice index between FMT reconstruction results and 2D fluorescence images of frozen sections was calculated and listed in Table VI. Different from the simulation experiments, IPS obtained the lowest average Dice (0.45), owning to the over-sparse problem. The average Dice given by SBRTV method (0.67) was close to that of KNN-LC network (0.74), but the over-smooth problem of SBRTV was serious. These results proved the practicability of KNN-LC network for the morphological reconstruction of probe distribution in glioma mouse models.

E. Reconstruction Time

To evaluate the reconstruction efficiency of KNN-LC network, the reconstruction time of different methods

TABLE VI
QUANTITATIVE RESULTS OF DICE IN *in Vivo* EXPERIMENTS

Method	Mouse 1	Mouse 2	Mouse 3	Mean ± SD
SBRTV	0.73	0.67	0.61	0.67 ± 0.06
IPS	0.36	0.45	0.54	0.45 ± 0.09
KNN-LC	0.76	0.77	0.71	0.74 ± 0.03

was calculated. For FMT reconstruction, both model-based and data-driven methods take lots of time to do preparations. Model-based methods need construct system matrix by finite element analysis, whereas data-driven methods need collect training data and train network. However, the reconstruction using well trained network is particularly faster than iterative calculation of model-based methods. In this study, only the test time of data-driven methods and the iterative calculation time were collected for comparisons. The mean ± SD of the reconstruction time given by IPS (0.167 ± 0.001 s) and KNN-LC network (0.169 ± 0.005 s) were close, which were significantly shorter than that of SBRTV (137.2 ± 3.56 s). These results revealed the superiority of data-driven methods in fast FMT reconstruction.

IV. CONCLUSION AND DISCUSSION

In this paper, a novel KNN-LC network was proposed to achieve fast morphological reconstruction of FMT by learning the mapping relation between the surface photon intensity and the distribution of fluorescent source directly. Based on the priori knowledge that the adjacent voxels (not including boundary voxels) tend to have similar fluorescence intensity, we built a KNN-LC network by constructing a LC sub-network based on K-nearest neighbor and cascading it behind a FC sub-network. With the help of residual learning, KNN-LC network learned local information of reconstructed results and improved the morphological reconstruction of FMT.

To verify the performance of KNN-LC network, we implemented dual-source and big-source simulation studies. The conventional model-based SBRTV method and the machine learning-based IPS method were adopted for comparisons. All reconstruction results demonstrated that KNN-LC network obtained the most accurate source localization and the best morphology recovery of fluorescent sources. To further evaluate the practicability of KNN-LC network, we performed *in vivo* experiments in three glioma mouse models. Consistent with our numerical simulation studies, KNN-LC network obtained the best morphological reconstruction of probe distribution in biological tissue. The average Dice index of KNN-LC network was 0.74, which was higher than that of the other two methods. These results revealed that KNN-LC network obtained accurate FMT reconstruction of probe distribution in glioma mouse models.

To our best knowledge, this is the first research that achieved such accurate morphological FMT reconstruction based on machine learning. Benefiting from the superiority of machine learning, FMT holds great potential for fast imaging of fluorescence probe distribution. Besides, KNN-LC network completely abandoned the photon propagation modeling and the inverse problem solving. It directly learned the mapping relation between the surface photon intensity and the distribution of fluorescent source from thousands of simulation samples. Our *in vivo* experiments demonstrated the feasibility of KNN-LC network for visualizing fluorescence probe distribution inside biological tissue.

However, there are still some limitations of KNN-LC network. The major drawback of KNN-LC network is the utilization of the standard mesh. The registration between the standard mesh and *in vivo* structural data might bring extra error in FMT reconstruction. Besides, the value of the nearest neighbor K was set as a constant in each LC layer based on parameter test. An adaptive strategy for selecting K is necessary to further improve the performance of KNN-LC network, which will be performed in our future research.

In conclusion, a data-driven strategy using KNN-LC network was proposed for morphological reconstruction of FMT. It achieved accurate source localization and morphology recovery of FMT in a short time. We believe that this novel method holds great potential for improving the performance of FMT and promoting the application of FMT for *in vivo* biological research.

ACKNOWLEDGMENT

The author would like to thank Yu An and Lin Yin for the assistance of *in vivo* experiments.

REFERENCES

[1] R. Weissleder, C.-H. Tung, U. Mahmood, and A. Bogdanov, "*In vivo* imaging of tumors with protease-activated near-infrared fluorescent probes," *Nature Biotechnol.*, vol. 17, no. 4, pp. 375–378, Apr. 1999.
[2] R. Weissleder, "Scaling down imaging: Molecular mapping of cancer in mice," *Nature Rev. Cancer*, vol. 2, no. 1, pp. 11–18, Jan. 2002.
[3] V. Ntziachristos, C. Bremer, and R. Weissleder, "Fluorescence imaging with near-infrared light: New technological advances that enable *in vivo* molecular imaging," *Eur. Radiol.*, vol. 13, no. 1, pp. 195–208, Jan. 2003.
[4] P. Mohajerani and V. Ntziachristos, "An inversion scheme for hybrid fluorescence molecular tomography using a fuzzy inference system," *IEEE Trans. Med. Imag.*, vol. 35, no. 2, pp. 381–390, Feb. 2016.
[5] S. Zhang *et al.*, "Robust reconstruction of fluorescence molecular tomography based on sparsity adaptive correntropy matching pursuit method for stem cell distribution," *IEEE Trans. Med. Imag.*, vol. 37, no. 10, pp. 2176–2184, Oct. 2018.
[6] Y. Gao, K. Wang, S. Jiang, Y. Liu, T. Ai, and J. Tian, "Bioluminescence tomography based on Gaussian weighted Laplace prior regularization for *in vivo* morphological imaging of glioma," *IEEE Trans. Med. Imag.*, vol. 36, no. 11, pp. 2343–2354, Nov. 2017.
[7] R. B. Schulz *et al.*, "Hybrid system for simultaneous fluorescence and X-ray computed tomography," *IEEE Trans. Med. Imag.*, vol. 29, no. 2, pp. 465–473, Feb. 2010.
[8] H. Liu *et al.*, "Multispectral hybrid cerenkov luminescence tomography based on the finite element SPn method," *J. Biomed. Opt.*, vol. 20, no. 8, Aug. 2015, Art. no. 086007.
[9] X. He, H. Guo, J. Yu, X. Zhang, and Y. Hou, "Effective and robust approach for fluorescence molecular tomography based on CoSaMP and SP3 model," *J. Innov. Opt. Health Sci.*, vol. 9, no. 6, Nov. 2016, Art. no. 1650024.
[10] Y. An *et al.*, "A novel region reconstruction method for fluorescence molecular tomography," *IEEE Trans. Biomed. Eng.*, vol. 62, no. 7, pp. 1818–1826, Jul. 2015.
[11] R. Baikejiang, Y. Zhao, B. Z. Fite, K. W. Ferrara, and C. Li, "Anatomical image-guided fluorescence molecular tomography reconstruction using kernel method," *J. Biomed. Opt.*, vol. 22, no. 5, May 2017, Art. no. 055001.
[12] X. Cao *et al.*, "An adaptive tikhonov regularization method for fluorescence molecular tomography," *Med. Biol. Eng. Comput.*, vol. 51, no. 8, pp. 849–858, Aug. 2013.
[13] J. Dutta, S. Ahn, C. Li, S. R. Cherry, and R. M. Leahy, "Joint L1 and total variation regularization for fluorescence molecular tomography," *Phys. Med. Biol.*, vol. 57, no. 6, pp. 1459–1476, Mar. 2012.

[14] E. Edjlali and Y. Bérubé-Lauzière, "L_q–L_p optimization for multigrid fluorescence tomography of small animals using simplified spherical harmonics," *J. Quant. Spectrosc. Radiat. Transf.*, vol. 205, pp. 163–173, Jan. 2018.

[15] H. Meng, K. Wang, Y. Gao, Y. Jin, X. Ma, and J. Tian, "Adaptive Gaussian weighted Laplace prior regularization enables accurate morphological reconstruction in fluorescence molecular tomography," *IEEE Trans. Med. Imag.*, vol. 38, no. 12, pp. 2726–2734, Dec. 2019.

[16] D. Han *et al.*, "Efficient reconstruction method for L1 regularization in fluorescence molecular tomography," *Appl. Opt.*, vol. 49, no. 36, p. 6930, Dec. 2010.

[17] Y. Gao, K. Wang, Y. An, S. Jiang, H. Meng, and J. Tian, "Nonmodel-based bioluminescence tomography using a machine-learning reconstruction strategy," *Optica*, vol. 5, no. 11, p. 1451, Nov. 2018.

[18] C. Huang, H. Meng, Y. Gao, S. Jiang, K. Wang, and J. Tian, "Fast and robust reconstruction method for fluorescence molecular tomography based on deep neural network," *Proc. SPIE*, vol. 10881, Mar. 2019, Art. no. 108811K.

[19] L. Guo, F. Liu, C. Cai, J. Liu, and G. Zhang, "3D deep encoder–decoder network for fluorescence molecular tomography," *Opt. Lett.*, vol. 44, no. 8, p. 1892, Apr. 2019.

[20] S. Ren *et al.*, "Multi-atlas registration and adaptive hexahedral voxel discretization for fast bioluminescence tomography," *Biomed. Opt. Express*, vol. 7, no. 4, p. 1549, Apr. 2016.

[21] A. Behrooz, H.-M. Zhou, A. A. Eftekhar, and A. Adibi, "Total variation regularization for 3D reconstruction in fluorescence tomography: Experimental phantom studies," *Appl. Opt.*, vol. 51, no. 34, p. 8216, Dec. 2012.

[22] J. Shi, F. Liu, J. Zhang, J. Luo, and J. Bai, "Fluorescence molecular tomography reconstruction via discrete cosine transform-based regularization," *J. Biomed. Opt.*, vol. 20, no. 5, May 2015, Art. no. 055004.

[23] D. Wang, X. Liu, Y. Chen, and J. Bai, "A novel Finite-Element-Based algorithm for fluorescence molecular tomography of heterogeneous media," *IEEE Trans. Inf. Technol. Biomed.*, vol. 13, no. 5, pp. 766–773, Sep. 2009.

[24] A. X. Cong and G. Wang, "A finite-element-based reconstruction method for 3D fluorescence tomography," *Opt. Express*, vol. 13, no. 24, p. 9847, 2005.

[25] G. Wang, J. C. Ye, K. Mueller, and J. A. Fessler, "Image reconstruction is a new frontier of machine learning," *IEEE Trans. Med. Imag.*, vol. 37, no. 6, pp. 1289–1296, Jun. 2018.

[26] A. Krizhevsky, I. Sutskever, and G. E. Hinton, "ImageNet classification with deep convolutional neural networks," in *Proc. Int. Conf. Neural Inf. Process. Syst.*, 2012, pp. 1097–1105.

[27] D. Han *et al.*, "A fast reconstruction algorithm for fluorescence molecular tomography with sparsity regularization," *Opt. Express*, vol. 18, no. 8, p. 8630, Apr. 2010.

[28] K. He, X. Zhang, S. Ren, and J. Sun, "Deep residual learning for image recognition," in *Proc. IEEE Conf. Comput. Vis. Pattern Recognit. (CVPR)*, Jun. 2016, pp. 770–778.

[29] V. H. Vu, "On the infeasibility of training neural networks with small mean-squared error," *IEEE Trans. Inf. Theory*, vol. 44, no. 7, pp. 2892–2900, 1998.

[30] D. P. Kingma and J. Ba, "Adam: A method for stochastic optimization," 2014, *arXiv:1412.6980*. [Online]. Available: http://arxiv.org/abs/1412.6980

[31] S. Bartel and A. H. Hielscher, "Monte Carlo simulations of the diffuse backscattering mueller matrix for highly scattering media," *Appl. Opt.*, vol. 39, no. 10, p. 1580, Apr. 2000.

[32] H. Li, J. Tian, and G. Wang, "Photon propagation model of *in vivo* bioluminescent imaging based on Monte Carlo," *J. Softw.*, vol. 15, pp. 1709–1719, 2004.

[33] L. Wang, S. L. Jacques, and L. Zheng, "MCML–Monte Carlo modeling of light transport in multi-layered tissues," *Comput. Methods Programs Biomed.*, vol. 47, no. 2, pp. 131–146, Jul. 1995.

[34] J. Tian, J. Liang, X. Chen, and X. Qu, "Molecular optical simulation environment," in *Molecular Imaging: Fundamentals and Applications*. Berlin, Germany: Springer, 2013, pp. 15–46.

[35] S. L. Jacques, "Optical properties of biological tissues: A review," *Phys. Med. Biol.*, vol. 58, no. 11, pp. R37–R61, Jun. 2013.

[36] K. Wang *et al.*, "Optical molecular imaging frontiers in oncology: The pursuit of accuracy and sensitivity," *Engineering*, vol. 1, no. 3, pp. 309–323, Sep. 2015.

[37] S. Jiang *et al.*, "Novel l_2,1-norm optimization method for fluorescence molecular tomography reconstruction," *Biomed. Opt. Express*, vol. 7, no. 6, p. 2342, Jun. 2016.

[38] F. Maes, A. Collignon, D. Vandermeulen, G. Marchal, and P. Suetens, "Multimodality image registration by maximization of mutual information," *IEEE Trans. Med. Imag.*, vol. 16, no. 2, pp. 187–198, Apr. 1997.